

Insight into the Decomposition Mechanism of Donor–Acceptor Complexes of EH_2 (E = Ge and Sn) and Access to Germanium Thin Films from Solution

Jocelyn Sinclair, Guoliang Dai, Robert McDonald, Michael J. Ferguson, Alex Brown,* and Eric Rivard*

Cite This: <https://dx.doi.org/10.1021/acs.inorgchem.0c01492>

Read Online

ACCESS |

Metrics & More

Article Recommendations

Supporting Information

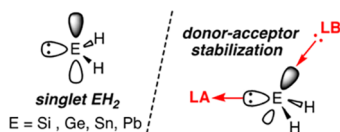
ABSTRACT: Electron-donating *N*-heterocyclic carbenes (Lewis bases, LB) and electron-accepting Lewis acids (LA) have been used in tandem to yield donor–acceptor complexes of inorganic tetrelenes $\text{LB}\cdot\text{EH}_2\cdot\text{LA}$ (E = Si, Ge, and Sn). Herein, we introduce the new germanium (II) dihydride adducts $\text{ImMe}_2\cdot\text{GeH}_2\cdot\text{BH}_3$ ($\text{ImMe}_2 = (\text{HCNMe})_2\text{C}:$) and $\text{Im}^i\text{Pr}_2\text{Me}_2\cdot\text{GeH}_2\cdot\text{BH}_3$ ($\text{Im}^i\text{Pr}_2\text{Me}_2 = (\text{MeCN}^i\text{Pr})_2\text{C}:$), with the former complex containing nearly 40 wt % germanium. The thermal release of bulk germanium from $\text{ImMe}_2\cdot\text{GeH}_2\cdot\text{BH}_3$ (and its deuterated isotopologue $\text{ImMe}_2\cdot\text{GeD}_2\cdot\text{BD}_3$) was examined in solution, and a combined kinetic and computational investigation was undertaken to probe the mechanism by which Ge is liberated. Moreover, the thermolysis of $\text{ImMe}_2\cdot\text{GeH}_2\cdot\text{BH}_3$ in solution cleanly affords conformal nanodimensional layers of germanium as thin films of variable thicknesses (20–70 nm) on silicon wafers. We also conducted a computational investigation into potential decomposition pathways for the germanium(II)- and tin(II)-dihydride complexes $\text{NHC}\cdot\text{EH}_2\cdot\text{BH}_3$ ($\text{NHC} = [(\text{HCNR})_2\text{C}:]$; R = 2,6- i -Pr $_2$ C $_6$ H $_3$ (Dipp), Me, and H; and E = Ge and Sn). Overall, this study introduces a mild and convenient solution-only protocol for the deposition of thin films of Ge, a widely used semiconductor in materials research and industry.



INTRODUCTION

Inorganic tetrelenes EH_2 (E = Si, Ge, Sn, and Pb) are highly reactive species that can be generated and trapped with sophisticated low-temperature matrix techniques (often < -200 °C).¹ As shown in Chart 1, these main group species adopt

Chart 1. Depiction of the Frontier Orbitals in Inorganic Tetrelenes (EH_2 ; E = Si, Ge, Sn, and Pb) and their Stabilization via Donor–Acceptor (Lewis Base or Acid, LB or LA) Coordination

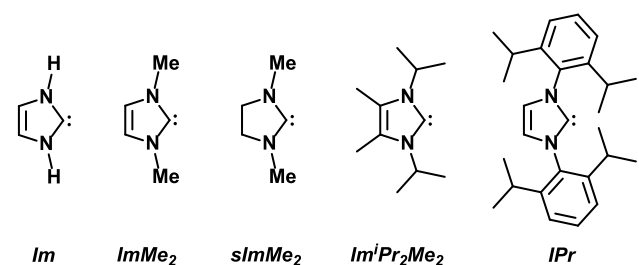


singlet electronic ground states, leading to a dual electron-accepting and electron-donating character. Group 14 element dihydrides are of considerable fundamental interest,² due in part to the role of SiH_2 and GeH_2 as key intermediates in the chemical vapor deposition (CVD) of bulk Si and Ge from gaseous tetrelanes EH_4 .³ While methylene-type (CH_2) reactivity can be coaxed from both metal (L_nMCH_2)⁴ and nonmetal (H_2CN_2)⁵ precursors, compounds bearing heavier element EH_2 reactivity are much scarcer.⁶ In 2009, the Rivard group prepared the first isolable complex of GeH_2 in the form of the Ge(II) adduct $\text{IPr}\cdot\text{GeH}_2\cdot\text{BH}_3$ ($\text{IPr} = [(\text{HCNDipp})_2\text{C}:]$

and $\text{Dipp} = 2,6\text{-}i\text{-Pr}_2\text{C}_6\text{H}_3$).⁷ This donor–acceptor stabilization approach involves coordinating reactive main group fragments (such as GeH_2) between Lewis basic (LB) and Lewis acidic (LA) entities (Chart 1).^{8,9} Subsequently, this general donor–acceptor protocol provided access to various isolable complexes of inorganic tetrelenes EH_2 and ethylenes H_2EEH_2 (E = Si, Ge, and Sn).¹⁰ Of added note, $\text{LB}\cdot\text{GeH}_2\cdot\text{LA}$ complexes were shown to be precursors to luminescent Ge nanoparticles upon microwave heating of the complexes to 190 °C in organic solvents.¹¹ For comparison, this element deposition procedure is much milder than the widely used gas phase decomposition of toxic GeH_4 (>450 °C) to elemental Ge and dihydrogen.^{3c}

Herein, new germanium-rich $\text{NHC}\cdot\text{GeH}_2\cdot\text{BH}_3$ adducts ($\text{NHC} = \text{N}$ -heterocyclic carbene) are introduced with nearly a 40 wt % of Ge. A number of different NHCs were investigated experimentally and computationally (Chart 2) en route to the isolation of the new reported complexes. Moreover, we show that $\text{ImMe}_2\cdot\text{GeH}_2\cdot\text{BH}_3$ ($\text{ImMe}_2 = (\text{HCNMe})_2\text{C}:$) can cleanly deposit germanium as 20 to 70

Received: May 22, 2020

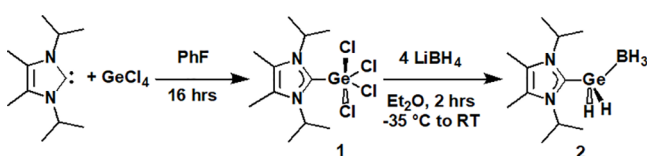
Chart 2. *N*-Heterocyclic Carbenes Investigated in This Study

nm thick films onto various substrates.^{12,13} While $\text{ImMe}_2 \cdot \text{GeH}_2 \cdot \text{BH}_3$ does not have the required volatility to enable its use in CVD, the use of this complex to yield nanometer-thick Ge coatings via an entirely solution-phase and low-temperature approach has distinct advantages over pre-existing routes to Ge films, including the ability to deposit Ge onto thermally sensitive and nonconducting substrates without the need for high vacuum chambers or electrochemical apparatuses.^{13d-f} In addition to these promising new results, an important question remained unanswered: what is the mechanism of EH_2 release from our donor–acceptor complexes? Does the first step involve LB-E or E-LA bond cleavage, or does a competing process, such as a 1,2-hydrogen shift from the tetrel element (E) to an *N*-heterocyclic carbene carbon center,¹⁴ occur en route to element deposition? Due to the transient nature of the EH_2 species,¹⁵ a combined experimental (kinetics) and computational approach was used to evaluate possible decomposition pathways available to $\text{ImMe}_2 \cdot \text{GeH}_2 \cdot \text{BH}_3$. We also used computations to evaluate the decomposition energetics associated with the E(II) dihydride adducts $\text{NHC} \cdot \text{EH}_2 \cdot \text{BH}_3$ (NHC = IPr, ImMe_2 , or $[(\text{HCNH})_2\text{C}]$) (Im) and E = Ge or Sn).

RESULTS AND DISCUSSION

NHC-GeH₂-BH₃ Adducts with Increased Germanium Content. Given the successful preparation of $\text{IPr} \cdot \text{GeH}_2 \cdot \text{BH}_3$,⁷ and the subsequent application of similar donor–acceptor LB-GeH₂-BH₃ compounds for the deposition of bulk and nanodimensional germanium,¹¹ we leveraged the functional group tunability of NHCs to pursue higher germanium weight-content precursors. The first carbene donor explored in this study, $\text{Im}^i\text{Pr}_2\text{Me}_2$ ($[(\text{MeCN}^i\text{Pr})_2\text{C}]$), made an early debut in *N*-heterocyclic carbene chemistry¹⁶ and is a ligand commonly employed for Group 14 element halides and alkoxides.¹⁷ It also has half the molecular weight of IPr. Moreover, $\text{Im}^i\text{Pr}_2\text{Me}_2$ is a useful supporting ligand for copper atomic layer deposition (ALD) as it helps impart good thermal stability and high volatility to the Cu complexes involved.¹⁸

The target Ge(II) dihydride complex $\text{Im}^i\text{Pr}_2\text{Me}_2 \cdot \text{GeH}_2 \cdot \text{BH}_3$ (**2**) was prepared by combining the new Ge(IV) halide adduct $\text{Im}^i\text{Pr}_2\text{Me}_2 \cdot \text{GeCl}_4$ (**1**, made from free $\text{Im}^i\text{Pr}_2\text{Me}_2$ and GeCl_4)¹⁹ with excess $\text{Li}[\text{BH}_4]$ (Scheme 1). A related *in situ* Ge(IV) to

Scheme 1. Synthesis of $\text{Im}^i\text{Pr}_2\text{Me}_2 \cdot \text{GeH}_2 \cdot \text{BH}_3$ (**2**)

Ge(II) reduction and Ge–Cl to Ge–H metathesis procedure was used in our group to generate $\text{IPr} \cdot \text{GeH}_2 \cdot \text{BH}_3$.²⁰ Unlike its bulkier IPr congener $\text{IPr} \cdot \text{GeH}_2 \cdot \text{BH}_3$, the less-hindered adduct $\text{Im}^i\text{Pr}_2\text{Me}_2 \cdot \text{GeH}_2 \cdot \text{BH}_3$ (**2**) is prone to decomposition in solution, resulting in the formation of byproducts containing the imidazolium cation $[\text{Im}^i\text{Pr}_2\text{Me}_2\text{-H}]^+$. As these charged byproducts possess very similar solubilities to the GeH_2 complex **2**, samples of $\text{Im}^i\text{Pr}_2\text{Me}_2 \cdot \text{GeH}_2 \cdot \text{BH}_3$ (**2**) could only be obtained with a bulk purity of ca. 80%.¹⁹ From a crude sample of **2** we were able to select crystals suitable for single-crystal X-ray crystallographic analysis. The quality of the resulting crystallographic data was sufficient to allow for the full refinement of all boron- and germanium-bound hydrides (Figure 1a), leading to Ge–H bond lengths (1.43(2) and 1.48(2) Å) that are within the same range as those reported for $\text{IPr} \cdot \text{GeH}_2 \cdot \text{BH}_3$.⁷ The Ge–B distance (2.073(2) Å) in **2** is similar in length to that of the corresponding distance in $\text{IPr} \cdot \text{GeH}_2 \cdot \text{BH}_3$ (2.053(3) Å).⁷ The adjacent $\text{C}_{\text{NHC}}\text{-Ge}$ bond length in $\text{Im}^i\text{Pr}_2\text{Me}_2 \cdot \text{GeH}_2 \cdot \text{BH}_3$ (**2**) is 2.013(2) Å and is shorter than the $\text{C}_{\text{NHC}}\text{-Ge}$ interaction found in Baines' Ge(II) dichloride adduct $\text{Im}^i\text{Pr}_2\text{Me}_2 \cdot \text{GeCl}_2$ (2.106(3) Å).²¹

Given the challenges in obtaining pure $\text{Im}^i\text{Pr}_2\text{Me}_2 \cdot \text{GeH}_2 \cdot \text{BH}_3$ (**2**), we prepared the known saturated NHC complex $\text{sImMe}_2 \cdot \text{GeCl}_4$ (**3**)²² [$\text{sImMe}_2 = (\text{H}_2\text{CNMe})_2\text{C}$] from a C–Cl insertion reaction involving Cl_2Ge -dioxane and then explored the reactivity of **3** with $\text{Li}[\text{BH}_4]$ (Scheme 2). Despite careful control of the reaction temperature (from -35 °C to room temperature), the main product isolated was invariably the known *trans* isomer²³ of the dihydroaminal-bis(borane) adduct $\{[\text{H}_2\text{CNMe}(\text{BH}_3)]_2\text{CH}_2\}$ (**4**) (Scheme 2). The formation of **4** was accompanied by gray and white solids on the walls of the reaction vessel, which is consistent with the formation of bulk germanium and lithium chloride. Compound **4** was also isolated directly from the reaction between 2-chloro-1,3-dimethylimidazolium chloride and $\text{Li}[\text{BH}_4]$ (Scheme 2).

Our search for a new, stable, and low-weight germanium-rich NHC-GeH₂-BH₃ complex successfully ended with the high yield preparation of $\text{ImMe}_2 \cdot \text{GeH}_2 \cdot \text{BH}_3$ ($\text{ImMe}_2 = [(\text{HCNMe})_2\text{C}]$). Our route to this Ge(II) dihydride complex (Scheme 3) involved generation of the free carbene ImMe_2 *in situ*,²⁴ followed by the addition of a THF solution of this carbene to Cl_2Ge -dioxane to afford the new adduct $\text{ImMe}_2 \cdot \text{GeCl}_2$ (**5**); notably, prior computational studies indicated that the precursor complex **5** should be stable.²⁵ Crystals of $\text{ImMe}_2 \cdot \text{GeCl}_2$ (**5**) suitable for X-ray crystallography (Figure S43)¹⁹ were obtained by cooling a THF solution of this Ge(II) adduct to -35 °C. $\text{ImMe}_2 \cdot \text{GeH}_2 \cdot \text{BH}_3$ (**6**) was then prepared by combining slurries of $\text{ImMe}_2 \cdot \text{GeCl}_2$ and $\text{Li}[\text{BH}_4]$ in Et_2O , followed by vigorously stirring the reaction mixture at room temperature for 2 h (Scheme 3). After exchanging the solvent for fluorobenzene, X-ray quality crystals were subsequently grown at -35 °C, which conclusively identified the product as $\text{ImMe}_2 \cdot \text{GeH}_2 \cdot \text{BH}_3$ (**6**). As for the $\text{Im}^i\text{Pr}_2\text{Me}_2$ analogue **2**, the quality of the data allowed for the full refinement of the hydrogen atoms within the $-\text{GeH}_2\text{BH}_3$ unit (Figure 1b). The observed Ge–B distance in $\text{ImMe}_2 \cdot \text{GeH}_2 \cdot \text{BH}_3$ (**6**) (2.054(4) Å) is similar in length to that in the temperature-sensitive complex $\text{Im}^i\text{Pr}_2\text{Me}_2 \cdot \text{GeH}_2 \cdot \text{BH}_3$ (**2**) (2.073(2) Å), while the adjacent Ge– C_{NHC} bond length in **6** (1.996(2) Å) is shorter than those of the Ge– C_{NHC} linkages found in both $\text{IPr} \cdot \text{GeH}_2 \cdot \text{BH}_3$ (2.053(3) Å)⁷ and the precursor Ge(II) complex $\text{ImMe}_2 \cdot \text{GeCl}_2$ (2.069(4)–2.085(3) Å; the range from three different molecules in the asymmetric unit).¹⁹

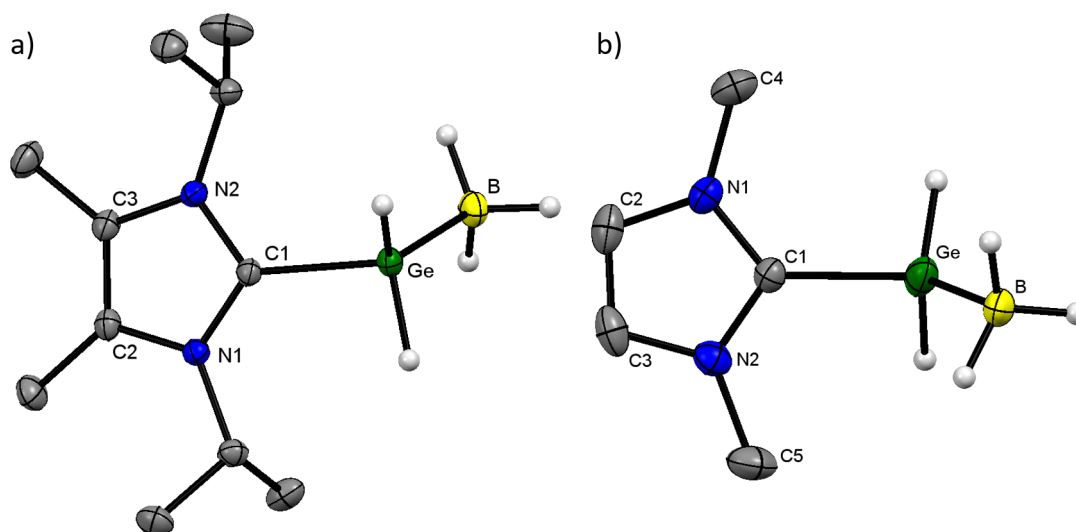
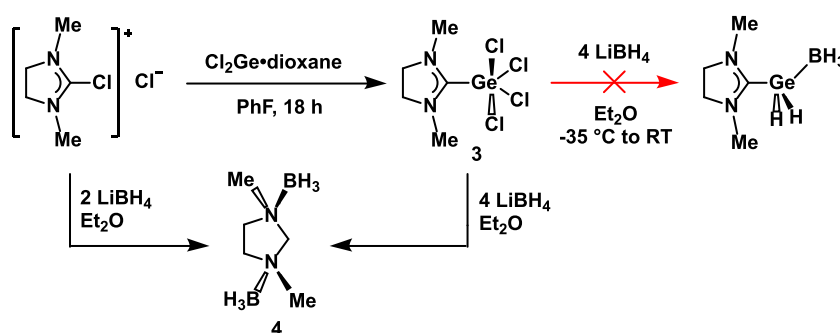
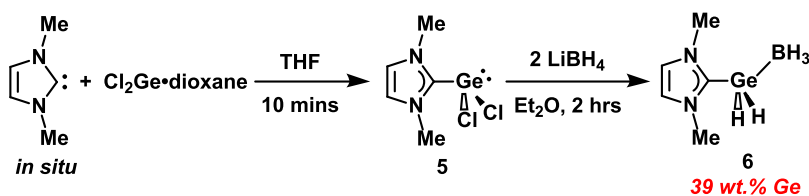


Figure 1. Crystal structures of (a) $\text{Im}^i\text{Pr}_2\text{Me}_2\cdot\text{GeH}_2\cdot\text{BH}_3$ (**2**, left) and (b) $\text{ImMe}_2\cdot\text{GeH}_2\cdot\text{BH}_3$ (**6**, right). Thermal ellipsoids are plotted at the 30% probability level with all carbene-based hydrogen atoms omitted for clarity. Selected bond lengths (Å) and angles ($^\circ$) for **2** are as follows: C1–Ge 2.013(2), Ge–B 2.073(2), Ge–H1 1.43(2), Ge–H2 1.48(2), N1–C1–N2 106.6(1), C1–Ge–B 110.21(7), and H–Ge–H 101(1). Selected bond lengths (Å) and angles ($^\circ$) for **6** are as follows: C1–Ge 1.996(2), Ge–B 2.054(4), Ge–H1 1.46(3), Ge–H2 1.62(2), N1–C1–N2 106.0(2), C1–Ge–B 113.5(1), and H–Ge–H: 101(1).

Scheme 2. Preparation of $\text{sImMe}_2\cdot\text{GeCl}_4$ (3**) and Subsequent Reactions with $\text{Li}[\text{BH}_4]$ to Form 1,3-Dimethyl-1,3-diazolidine Bis(borane) (**4**)**



Scheme 3. Synthesis of $\text{ImMe}_2\cdot\text{GeH}_2\cdot\text{BH}_3$ (6**)**



Controlled Release of Elemental Germanium from $\text{ImMe}_2\cdot\text{GeH}_2\cdot\text{BH}_3$ (6**).** We were then eager to see if $\text{ImMe}_2\cdot\text{GeH}_2\cdot\text{BH}_3$ (**6**) could yield bulk Ge after being heated in solution, and wanted to identify the nature of the byproducts formed to gain insight into the mechanism of decomposition. To start, a sample of $\text{ImMe}_2\cdot\text{GeH}_2\cdot\text{BH}_3$ (**6**) was heated to 100 $^\circ\text{C}$ (2 h) or 125 $^\circ\text{C}$ (3 days) under a static vacuum (ca. 2×10^{-2} mbar), and the products were examined by Raman spectroscopy (Figure 2). Analysis of the products formed after heating **6** to 100 $^\circ\text{C}$ (Figure 2, left) showed the appearance of the expected Ge–Ge peak²⁶ at 280 cm^{-1} for amorphous Ge coupled with a collective decrease in the intensity of the Raman peaks associated with **6**. The consumption of **6** was accompanied by the formation of the carbene–borane adduct $\text{ImMe}_2\cdot\text{BH}_3$. The photograph shown at the right of Figure 2

depicts the remaining sample after the thermolysis of **6** at 125 $^\circ\text{C}$ under N_2 (for 18 h) and illustrates the volatility of the decomposition byproduct $\text{ImMe}_2\cdot\text{BH}_3$, which crystallized on the walls of the upper (cooler) portion of the glass NMR tube; elemental Ge can be seen at the bottom of the tube. If the decomposition of **6** is repeated at 125 $^\circ\text{C}$ under a static vacuum of ca. 2×10^{-2} mbar for 3 days, the only nonvolatile species that remains (according to Raman spectroscopy) is amorphous Ge (Figure 2, left). The clean conversion of $\text{ImMe}_2\cdot\text{GeH}_2\cdot\text{BH}_3$ (**6**) to Ge and volatile $\text{ImMe}_2\cdot\text{BH}_3$ is promising, as the organic byproducts formed can be removed either by sublimation or washing with an organic solvent. Consistent with the Raman data in Figure 2, the deposited germanium from the solid state thermolysis of **6** was confirmed to be amorphous by powder X-ray diffraction (Figure S44).¹⁹

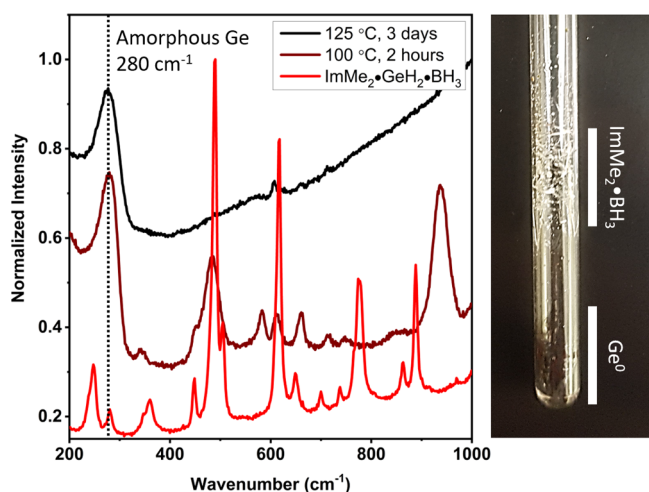


Figure 2. (left) Raman spectra associated with the decomposition of $\text{ImMe}_2\cdot\text{GeH}_2\cdot\text{BH}_3$ (**6**). Trials were conducted in the solid state under static vacuum. (right) Photograph of a sealed glass NMR tube under N_2 after the thermal decomposition of **6** at $125\text{ }^\circ\text{C}$ (18 h). Elemental Ge and crystalline $\text{ImMe}_2\cdot\text{BH}_3$ (also confirmed by ^1H NMR analysis)¹⁹ can be seen in the lower and upper portions of the tube, respectively.

To characterize the organic byproducts from the above-mentioned decomposition of $\text{ImMe}_2\cdot\text{GeH}_2\cdot\text{BH}_3$ (**6**), a sample of this adduct was then heated to reflux in C_6D_6 (external bath temperature of $100\text{ }^\circ\text{C}$; **caution, closed system**). ^1H and ^{11}B NMR spectroscopy after 48 h indicated the clean conversion of **6** into the known compound $\text{ImMe}_2\cdot\text{BH}_3$ ²⁷ (Figures S27 and S28).¹⁹ $\text{ImMe}_2\cdot\text{BH}_3$ was also independently synthesized to confirm its identity and to determine its thermal properties (*vide infra*).

The thermal properties of $\text{ImMe}_2\cdot\text{GeH}_2\cdot\text{BH}_3$ (**6**) were analyzed by differential scanning calorimetry (DSC) and thermogravimetric analysis (TGA), both of which were conducted at heating rates of $10\text{ }^\circ\text{C}/\text{min}$ under N_2 . A representative DSC trace is shown at the left in Figure 3 and reveals the onset of an endothermic event at $108\text{ }^\circ\text{C}$, agreeing well with the visually determined melting point of **6** ($103\text{--}105\text{ }^\circ\text{C}$). The subsequent exothermic event beginning at $118\text{ }^\circ\text{C}$ appears to be linked to the onset of Ge deposition, as thermal gravimetric analysis of $\text{ImMe}_2\cdot\text{GeH}_2\cdot\text{BH}_3$ (**6**) (Figure 3, middle) shows mass loss beginning at ca. $110\text{ }^\circ\text{C}$. TGA recorded another dip in mass near $150\text{ }^\circ\text{C}$, which corresponds with the tail end of the exothermic feature in the DSC of **6**. Continued heating of **6** up to $600\text{ }^\circ\text{C}$ results in the sublimation of the decomposition product $\text{ImMe}_2\cdot\text{BH}_3$ (*vide infra*), leading

to a residual mass of 49.6 wt % according to TGA. $\text{ImMe}_2\cdot\text{BH}_3$ was independently subjected to TGA (Figure 3, right) and the onset of its sublimation can be seen at $150\text{ }^\circ\text{C}$, aligning with features in the TGA trace of $\text{ImMe}_2\cdot\text{GeH}_2\cdot\text{BH}_3$ (**6**); for $\text{ImMe}_2\cdot\text{BH}_3$, sublimation reaches completion (100 wt % loss) at $290\text{ }^\circ\text{C}$. Given that $\text{ImMe}_2\cdot\text{GeH}_2\cdot\text{BH}_3$ (**6**) initially contains 39 wt % Ge, there is unaccounted mass left in the residue after TGA. At this stage, we are unsure as to the reason for the mass difference; however, we cannot rule out oxidation of the deposited Ge by traces of atmospheric oxygen. It may be posited also that some ImMe_2 or organic contaminants remain adhered to the surface of the deposited germanium, leading to the higher final mass yield. Energy dispersive X-ray (EDX) analyses of the residual samples of Ge after the decomposition of **6** in solution (*vide infra*) do not indicate the presence of nitrogen (Figure S48);¹⁹ however, the sensitivity of this technique to nitrogen is low.

The solution-phase deposition of Ge films was also carried out by the immersion of various substrates into solutions of $\text{ImMe}_2\cdot\text{GeH}_2\cdot\text{BH}_3$ (**6**) in toluene, followed by controlled heating. The samples were heated at $100\text{ }^\circ\text{C}$ for either 3 or 10 h, after which time the substrates were washed with benzene to remove the $\text{ImMe}_2\cdot\text{BH}_3$ byproduct. Gratifyingly, **6** was consistently able to deposit thin layers of elemental Ge onto a variety of substrates, including Si wafers (Figure 4) and glass wool (Figure S52).¹⁹ Deposition of thin films of germanium onto Si wafers yielded the best surface coverage, allowing for a reliable determination of the thickness of the deposited Ge by scratching the surface (post deposition, Figure 4a) and imaging of the exposed Ge film edges at an angle of 54° (Figure 4b).²⁸ EDX analysis (Figure 4c) illustrates the Ge deposited on the surface and the lower Ge signal where the deposited layer had been removed. The thicknesses of the deposited layers after heating for 10 h did not correlate with the concentration of **6** in solution (from 0.5 to $1.2 \times 10^{-2}\text{ M}$); however, all samples that were heated for this time period gave films with average thicknesses in the range of $17(2)\text{--}29(4)\text{ nm}$ (Table 1) with a similar morphology of overlapping hemispheroids. After samples of **6** were heated to $100\text{ }^\circ\text{C}$ for a shorter period of 3 h, the deposition of Ge still transpired to yield thicker layers (up to 70 nm).

One possible explanation for the formation of thin films at longer deposition times (Table 1) is an Ostwald ripening-type growth of the remaining suspended Ge nanoparticles in toluene at the expense of the surface-bound Ge.²⁹ Dynamic light scattering experiments revealed that the Ge particles in solution exhibited steady growth over time from a $187(28)\text{ nm}$ solvodynamic radius after 30 min to $773(21)\text{ nm}$ after 3 h

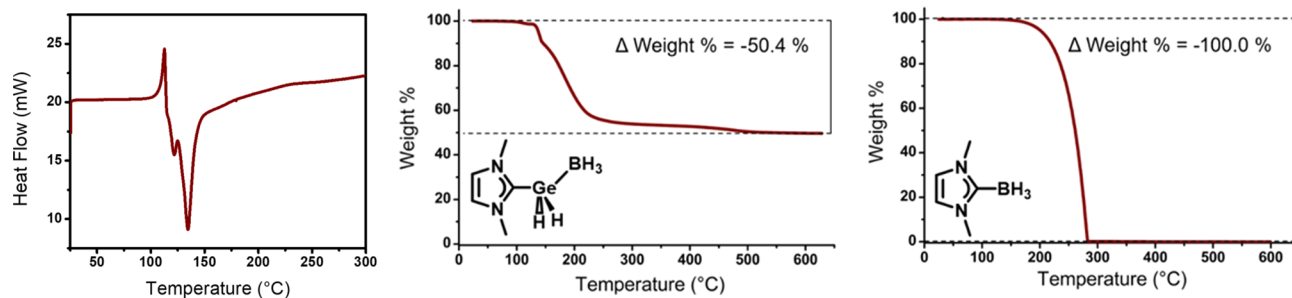


Figure 3. (left) DSC of $\text{ImMe}_2\cdot\text{GeH}_2\cdot\text{BH}_3$ (**6**) under a flow of N_2 , with a heating rate of $10\text{ }^\circ\text{C}/\text{min}$. TGA of (middle) $\text{ImMe}_2\cdot\text{GeH}_2\cdot\text{BH}_3$ (**6**) and (right) $\text{ImMe}_2\cdot\text{BH}_3$ conducted under a gentle flow of N_2 at a heating rate of $10\text{ }^\circ\text{C}/\text{min}$.

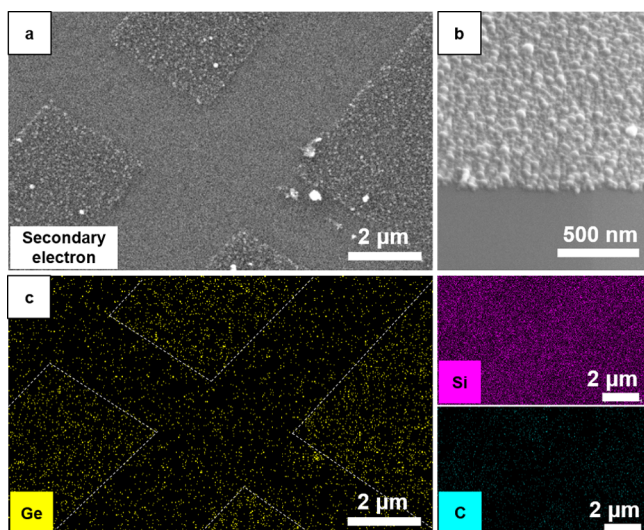


Figure 4. Ge layer deposited onto a Si wafer via the decomposition of $\text{ImMe}_2\text{-GeH}_2\text{-BH}_3$ (**6**) in toluene (at a concentration of 6.3×10^{-3} M for 10 h at 100°C). (a) Secondary electron SEM image of a Si wafer with the Ge layer scratched off in a pattern using a stainless-steel needle. (b) Micrograph taken at a 54° angle with respect to the electron beam to determine the layer thickness ($17(2)$ Å) at the edge of the scratch. (c) EDX mapping of the imaged section in **Figure 4a** showing a higher Ge signal in the unscratched areas along with a strong background of Si; some background C was also detected. Micrographs and EDX measurements were collected at 5 kV. Dotted lines on the Ge EDX map in **Figure 4c** are provided as guides for the eye.

Table 1. Layer Thickness Measurements of Amorphous Ge Deposited from **6 onto Si Wafers at 100°C in Toluene**

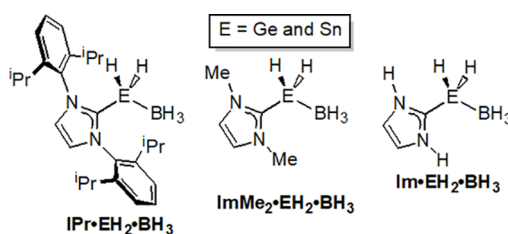
deposition time (h)	$[\text{ImMe}_2\text{-GeH}_2\text{-BH}_3]$ (M)	layer thickness (nm)
10	1.2×10^{-2}	20(4)
10	1.0×10^{-2}	22(4)
10	6.3×10^{-3}	17(2)
10	5.0×10^{-3}	29(4)
3	1.0×10^{-2}	73(12)
3	5.1×10^{-3}	40(7)

(**Table S5**),¹⁹ which provides support for the growth of Ge nanoparticles in solution over time. However, no direct evidence of a surface to nanoparticle germanium transfer was observed, which would have supported our Ostwald ripening postulate mentioned above. The walls of the reaction vessel were coated with an orange and red precipitate after Ge film deposition onto Si, indicating that Ge deposition is not exclusive to the Si substrate. Although a number of equilibria are possible between the solution, the precipitate, and the Ge film deposited on the substrate, it should be noted that the diameter of the hemispheroids deposited onto the Si wafer do not exceed ~ 150 nm (**Figure S47**),¹⁹ suggesting that larger particles of Ge are unstable on the Si surface and may be rinsed off during substrate processing. The Raman spectra of the deposited films consistently yield a characteristic broad peak for amorphous Ge, centered at 280 cm^{-1} (**Figure S51**).^{19,26} XPS identified the major deposited species to be elemental Ge (61%), with GeO and GeO₂ also present, likely due to the unavoidable exposure of the sample to oxygen before measurements were taken. Surface oxidation is to be expected due to the intermittent exposure of the sample to air prior to

XPS measurements; however, it should also be stated that XPS has a depth sensitivity of ~ 10 nm. Thus, it is likely that the bulk sample contains a higher ratio of Ge than is detected on the surface by XPS. An extremely low (0.48 atom %) amount of nitrogen was detected by the survey XPS on the substrates after deposition, supporting the earlier supposition that very little carbene (ImMe_2) remains bound to the surface of the deposited germanium even with the low deposition temperatures involved (**Figure S49**).¹⁹

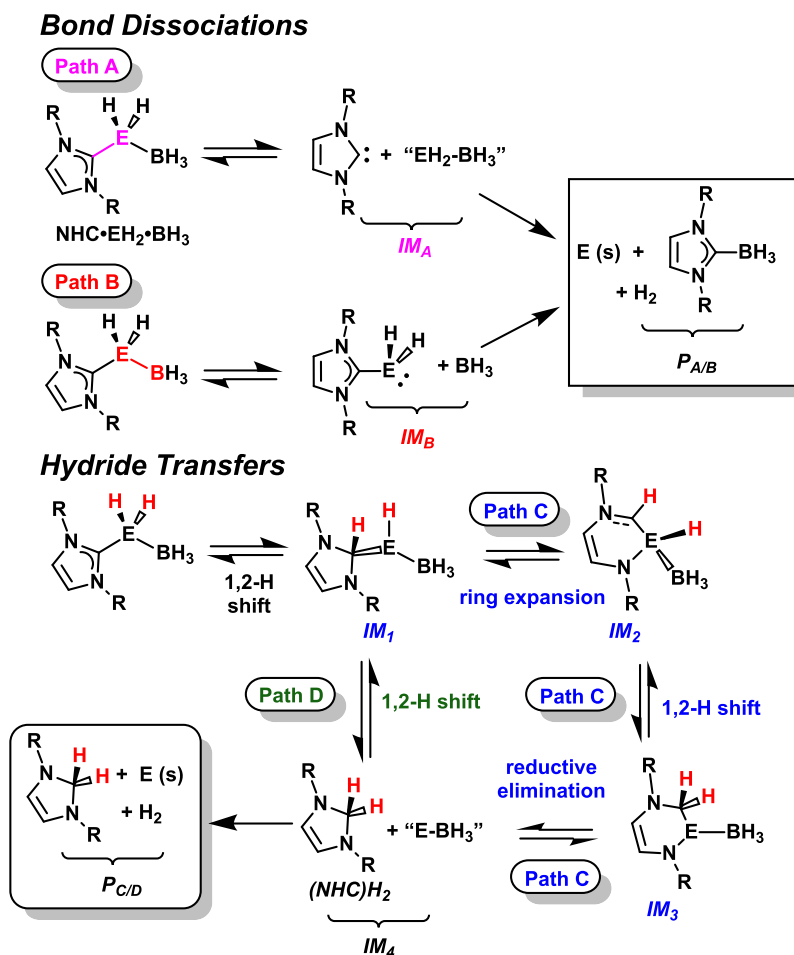
Computed Structures for NHC·EH₂·BH₃ Complexes (E = Ge and Sn). To probe the electronic and steric effects associated with the decomposition of our Ge(II) dihydride complexes, we first optimized the structures of the following three adducts: $\text{NHC}\cdot\text{GeH}_2\cdot\text{BH}_3$, where $\text{NHC} = [(\text{HCNR})_2\text{C}]$ and R = Dipp (IPr), Me (ImMe_2), or H (Im) (**Chart 3**). The

Chart 3. NHC·EH₂·BH₃ (E = Ge and Sn) Donor–Acceptor Adducts Examined Computationally in This Study



two most hindered complexes in the series, $\text{IPr}\cdot\text{GeH}_2\cdot\text{BH}_3$ ⁷ and $\text{ImMe}_2\cdot\text{GeH}_2\cdot\text{BH}_3$ (**6**), have been synthesized in the laboratory, while the parent system $\text{Im}\cdot\text{GeH}_2\cdot\text{BH}_3$ represents an experimentally unknown model complex. For comparison, the corresponding (unknown) Sn(II) dihydride complexes $\text{NHC}\cdot\text{SnH}_2\cdot\text{BH}_3$ were also studied computationally (**Chart 3**). Unless specified, all energies and geometrical parameters refer to those determined computationally with a THF polarizable continuum model (PCM); geometries for all structures are available in the **Supporting Information**.¹⁹ For all structures determined computationally in this work, the geometry optimizations were performed via density functional theory (DFT) calculations, using default convergence criteria, with the M06-2X functional.³⁰ In most computations, the cc-pVDZ basis set³¹ was used for all atoms except Sn, where the cc-pVDZ-PP basis set and a corresponding effective core potential were used.³¹ For Sn-containing compounds, this combination of basis sets will be referred to as cc-pVDZ-(PP). For the largest $\text{IPr}\cdot\text{GeH}_2\cdot\text{BH}_3$ complex, the 6-311+G(d) basis set³¹ was used.

Our computations show that NHC substitution has only a modest impact on the proximal $\text{C}_{\text{NHC}}\text{-Ge}$ bond length, with a ca. 0.04 Å bond elongation noted when the less hindered complex $\text{Im}\cdot\text{GeH}_2\cdot\text{BH}_3$ is compared to the Dipp-containing complex $\text{IPr}\cdot\text{GeH}_2\cdot\text{BH}_3$ (2.039 vs 2.074 Å). Notably, the $\text{C}_{\text{NHC}}\text{-Ge-B}$ bond angle widens from 100.0° (NHC = Im) to 116.3° (ImMe_2) to 125.5° (IPr) as the steric bulk of the NHC is increased. Within the $\text{NHC}\cdot\text{SnH}_2\cdot\text{BH}_3$ series,¹⁹ the computed $\text{C}_{\text{NHC}}\text{-Sn}$ bond length in $\text{IPr}\cdot\text{SnH}_2\cdot\text{BH}_3$ (2.369 Å) is significantly longer than that in $\text{Im}\cdot\text{SnH}_2\cdot\text{BH}_3$ (2.312 Å). The $\text{C}_{\text{NHC}}\text{-Sn-B}$ bond angles also increase from 91.5° to 109.6° to 123.9° when the NHC is altered from Im to ImMe_2 to IPr, respectively. Lastly, the nature of the N-bound substituents has a minimal impact on the coordinative E–B bond lengths, with all values within 0.01 Å of each other

Scheme 4. Computationally Investigated Pathways for NHC·EH₂·BH₃ Decomposition^a

^aPaths A and B represent heterolytic C_{NHC}-E and E-B bond cleavage, while paths C and D follow an initial common 1,2-hydride shift to generate a putative (NHCH)E(H)·BH₃ intermediate (IM₁).

among the GeH₂ and SnH₂ adduct series.¹⁹ Natural bond orbital (NBO) analysis showed that the C_{NHC}-E linkages in the NHC·EH₂·BH₃ adducts are substantially polarized toward the ligating NHC carbon (C_{NHC}). For example, the C_{NHC}-Ge bond in IPr·GeH₂·BH₃ has a single bond character with 76.3% of the electron density toward carbon while the Ge-B bond in IPr·GeH₂·BH₃ shows a slight polarization of electron density toward the Ge atom (53.5%).¹⁹

Computational Evaluation of Possible Decomposition Mechanisms for NHC·GeH₂·BH₃ Adducts. Given the above-mentioned ability of ImMe₂·GeH₂·BH₂ to yield elemental germanium upon mild thermolysis in either THF or toluene, the mechanism by which this process happens is of significant interest. Herein, two possible decomposition routes were examined for the NHC·EH₂·BH₃ adducts (E = Ge or Sn): (a) the stepwise dissociation of E-B and C_{NHC}-E bonds (or in the reverse order) to liberate EH₂ and eventually afford bulk Ge (or Sn), NHC·BH₃, and H₂ gas (paths A and B in Scheme 4) and (b) 1,2-hydride transfer (migration) routes that either involve carbene-ring expansion¹⁴ and the reductive elimination of Ge or Sn (path C in Scheme 4) or the direct formation of a dihydroaminal (NHC)H₂ by sequential Ge (or Sn) to C hydride transfers (path D). We also computed the Gibbs free energies associated with various intermediates and transition states along paths A-D, both in the gas phase and

with a THF polarizable continuum model (PCM). For the final E(g) to E(s) steps, we used the experimentally known Δ_fG for the gaseous elements,³² which are 335.9 and 267.3 kJ/mol for Ge(g) and Sn(g), respectively. The results determined at 298.15 K for paths A/B and C/D for ImMe₂·GeH₂·BH₃ (6) are summarized in Figures 5 and 6, respectively; corresponding results at 373.15 K (100 °C) in THF can be found as Figures S72 and S73 in the Supporting Information and demonstrate that all the reported free energy differences are modestly reduced. The corresponding energy profiles for the decomposition of the structurally related Im·GeH₂·BH₃ and IPr·GeH₂·BH₃ adducts can be found as Figures S57-S61 in the Supporting Information.¹⁹

Paths A and B: Direct Adduct Cleavage. The most direct route by which NHC·GeH₂·BH₃ adducts might decompose is via the initial heterolytic cleavage of a polar covalent (dative) C_{NHC}-Ge or Ge-B bond with the eventual formation of NHC·BH₃, elemental Ge, and H₂. Path A (Scheme 4) involves an initial C_{NHC}-Ge bond breakage, followed by Ge-B bond dissociation; path B (Scheme 4) begins with Ge-B bond dissociation, followed by C_{NHC}-Ge bond breakage. Both of these pathways then proceed by the coordination of BH₃ to NHC (yielding NHC·BH₃) and the concomitant decomposition of GeH₂ into Ge and H₂. As

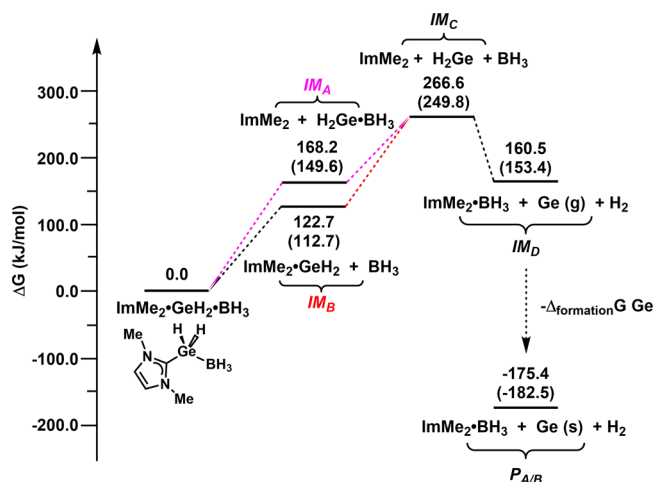


Figure 5. Computed Gibbs free energies (kJ/mol) associated with the intermediates formed in the decomposition of $\text{ImMe}_2\cdot\text{GeH}_2\cdot\text{BH}_3$ via path A (e.g., IM_A and $\text{P}_{A/B}$) and path B (e.g., IM_B and $\text{P}_{A/B}$) with a THF PCM; values in parentheses refer to gas-phase computations. Lowest energy states are plotted; in this case, IM_C contains H_2Ge in the singlet state, and IM_D is plotted containing $\text{Ge}(\text{g})$ (triplet) (Table S6).¹⁹ The Gibbs free energy of formation ($\Delta_f G$) for $\text{Ge}(\text{g})$ was taken as 335.9 kJ/mol.³²

before, each mechanism was examined in the gas phase and THF using a PCM.¹⁹

Path A involves the endoergic cleavage of a $\text{C}_{\text{NHC}}\text{--Ge}$ bond in $\text{ImMe}_2\cdot\text{GeH}_2\cdot\text{BH}_3$ (Figure 5) at a Gibbs free energy penalty of 168.2 kJ/mol in THF, which is slightly less favorable in comparison to the free energy cost of 149.6 kJ/mol in the gas phase. Next, Ge--B cleavage in the putative intermediate $\text{H}_2\text{Ge}\cdot\text{BH}_3$ is predicted to occur at a lower free energy change of 98.4 kJ/mol. Overall, the first step associated with path B is slightly more energetically favorable, given the lower free energy associated with the initial heterolytic Ge--B bond cleavage ($\Delta G = 122.7$ kJ/mol) in THF compared to that of the initial $\text{C}_{\text{NHC}}\text{--B}$ bond scission in path A (168.2 kJ/mol). Once the BH_3 group is liberated, scission of the remaining coordinative $\text{C}_{\text{NHC}}\text{--Ge}$ bond in the adduct $\text{ImMe}_2\cdot\text{GeH}_2$

occurs with a free energy change of 143.9 kJ/mol (in THF); thus, $\text{C}_{\text{NHC}}\text{--Ge}$ bond cleavage becomes slightly more endoergic in $\text{ImMe}_2\cdot\text{GeH}_2\cdot\text{BH}_3$ versus that in $\text{ImMe}_2\cdot\text{GeH}_2$, which partially explains our inability to isolate $\text{NHC}\cdot\text{GeH}_2$ complexes thus far in our laboratory. As outlined in Figures S57–S61 in the Supporting Information,¹⁹ similar energy trends for the decomposition of $\text{IPr}\cdot\text{GeH}_2\cdot\text{BH}_3$ and $\text{Im}\cdot\text{GeH}_2\cdot\text{BH}_3$ were found, and a preference for path B was noted.

Alternate Decomposition Routes for $\text{NHC}\cdot\text{GeH}_2\cdot\text{BH}_3$ Adducts: Ring Expansion (Path C) and Direct Hydrogen Transfer (Path D) Mechanisms.

Path C is outlined in Scheme 4 and starts with a 1,2-hydride shift from germanium to the carbene carbon (C_{NHC}) to give $(\text{NHCH})\text{GeH}\cdot\text{BH}_3$ (IM_1), followed by a carbene ring expansion to eventually give intermediate IM_3 . Path C ends with the formal reductive elimination of the dihydroaminal $(\text{NHC})\text{H}_2$ from the ring-expanded intermediate IM_3 , releasing “ $\text{Ge}\cdot\text{BH}_3$ ” to later form elemental Ge and BH_3 as coproducts ($\text{P}_{C/D}$, Scheme 4). For $\text{ImMe}_2\cdot\text{GeH}_2\cdot\text{BH}_3$ (Figure 6), the first step in path C, hydride migration from Ge to C_{NHC} involves a relatively high Gibbs free energy of activation of 218.8 kJ/mol; therefore, path C is already more energetically unfavorable at this stage for the decomposition of $\text{ImMe}_2\cdot\text{GeH}_2\cdot\text{BH}_3$ in relation to paths A and B by ca. 70–100 kJ/mol. The next step in path C involves carbene ring expansion,¹⁴ where a Ge atom inserts into a C--N bond to yield a GeN_2C_2 six-membered ring intermediate IM_2 (Scheme 4 and Figure 6). This ring expansion process is accompanied by a modest free energy of activation (via TS_{1-2}) of $\Delta G^\ddagger = 39.4$ kJ/mol, which is energetically more favorable by about 180 kJ/mol compared to that of the initial 1,2-hydride shift. From IM_2 , another 1,2-hydrogen shift (via TS_{2-3}) was modeled to yield the cyclic intermediate IM_3 ($\Delta G^\ddagger = 106.8$ kJ/mol). The last computed step in this mechanism involves the direct reductive elimination of the dihydroaminal $(\text{ImMe}_2)\text{H}_2$ from IM_3 , producing the putative species “ $\text{Ge}\cdot\text{BH}_3$ ”; this step is the least favorable of path C, with a large free energy of activation of 230.3 kJ/mol (via TS_{3-4}).

We also probed a direct hydrogen transfer mechanism (path D) in which two direct Ge to C_{NHC} hydride transfer processes occur to release the dihydroaminal $(\text{ImMe}_2)\text{H}_2$ without a

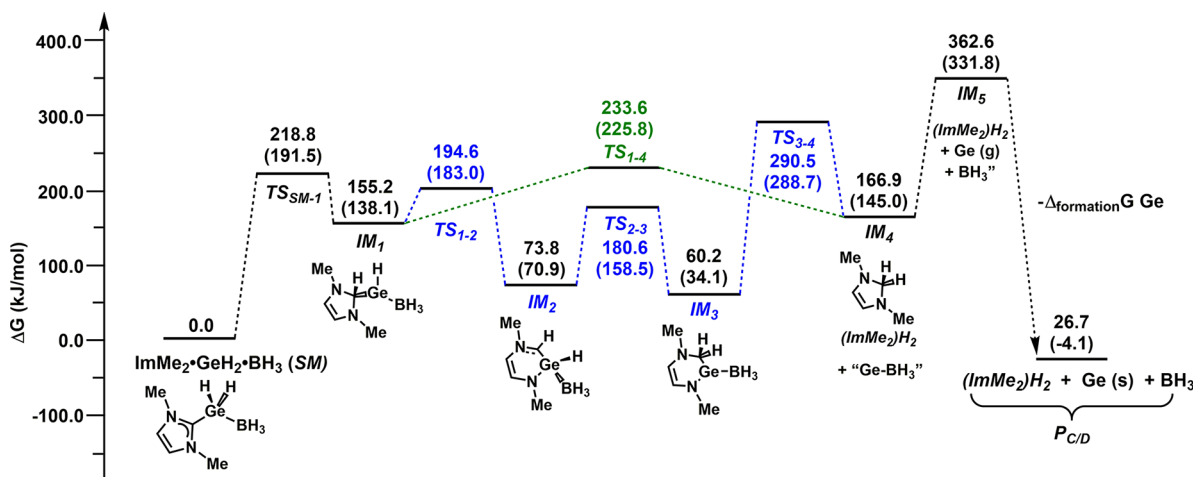


Figure 6. Computed Gibbs free energies in kJ/mol associated with the intermediates formed in the decomposition of $\text{ImMe}_2\cdot\text{GeH}_2\cdot\text{BH}_3$ via path C (stepwise via $\text{IM}_1\text{--IM}_4$) and path D (via TS_{1-4}) with a THF PCM; values in parentheses refer to gas phase computations. Lowest energy states are plotted; in this case, IM_5 is plotted as containing $\text{Ge}(\text{g})$ (triplet) (see Table S6).¹⁹ The Gibbs free energy of formation ($\Delta_f G$) for $\text{Ge}(\text{g})$ was taken as 335.9 kJ/mol.³²

carbene ligand ring expansion. The first step in path D is exactly the same as in path C, with a 1,2-H shift from Ge to C_{NHC} to form $(\text{ImMe}_2\text{H})\text{GeH}\cdot\text{BH}_3$ (**IM**₁, Figure 6); to recap, this step has a large free energy of activation (in THF) of 218.8 kJ/mol. As summarized in Figure 6, path D then involves a second direct 1,2-hydrogen migration between Ge and C_{NHC} in **IM**₁ to form $(\text{ImMe}_2)_2\text{H}_2$ and “Ge·BH₃” (**IM**₄); this second 1,2-H shift has a computed free energy of activation of 78.4 kJ/mol (via **TS**₁₋₄). Once at the intermediate **IM**₄, path D follows a similar route as path C to eventually give the final decomposition products $(\text{ImMe}_2)_2\text{H}_2$, Ge(s) and BH₃ (**P**_{C/D} in Figure 6).

When rate-determining steps (RDSs) for paths A–D (note: the initial bond dissociations in paths A and B are barrierless, Figure S57) were calculated,¹⁹ the decomposition of $\text{ImMe}_2\cdot\text{GeH}_2\cdot\text{BH}_3$ was predicted to proceed via path B (with a free energy of activation for the RDS of 143.9 kJ/mol, Figure 5), with an associated barrier in the RDS for path A of 168.2 kJ/mol (Figure 5). The initial cleavage of the Ge–B bond in path B is the most energetically feasible initial step of the paths explored (A–D), with a free energy penalty of 122.7 kJ/mol in THF; the RDSs for paths C (230.3 kJ/mol) and D (218.8 kJ/mol) are energetically the highest of the series. In line with our computations, the thermal decomposition of $\text{ImMe}_2\cdot\text{GeH}_2\cdot\text{BH}_3$ does not yield any dihydroaminal ($(\text{ImMe}_2)_2\text{H}_2$); thus, the decomposition of the Ge(II) dihydride adducts via either path A or B appears to be the most plausible.

We also estimated the overall free energies associated with the formation of the $\text{ImMe}_2\cdot\text{GeH}_2\cdot\text{BH}_3$ decomposition products from paths A/B: $\text{ImMe}_2\cdot\text{BH}_3$, Ge(s), and H₂ (**P**_{A/B} in Scheme 4 and Figure 5). After taking the Gibbs free energy of formation for Ge(g) into consideration,³² an overall $\Delta_{\text{decomp}}G$ of -175.4 kJ/mol was estimated (-182.5 kJ/mol in the absence of solvent). For comparison, the free energy associated with $\text{ImMe}_2\cdot\text{GeH}_2\cdot\text{BH}_3$ decomposition via paths C/D to give $(\text{ImMe}_2)_2\text{H}_2$, Ge(s), and BH₃ was found to be unfavorable in THF, with an estimated $\Delta_{\text{decomp}}G$ of $+26.7$ kJ/mol (-4.1 kJ/mol in the absence of solvent, Figure 6). Thus far, our computational and experimental data suggest that $\text{NHC}\cdot\text{GeH}_2\cdot\text{BH}_3$ adducts likely decompose via either path A or B.

Computed Mechanisms for $\text{NHC}\cdot\text{SnH}_2\cdot\text{BH}_3$ Decomposition. We also computed the Gibbs free energies associated with the decomposition of the model Sn(II) dihydride complexes $\text{NHC}\cdot\text{SnH}_2\cdot\text{BH}_3$ ($\text{NHC} = \text{IPr}, \text{ImMe}_2$, and Im ; Chart 2). It should be stated that our attempts to prepare $\text{IPr}\cdot\text{SnH}_2\cdot\text{BH}_3$ afforded exclusively Sn metal, H₂, and $\text{IPr}\cdot\text{BH}_3$ ⁷ while the isolation of stable Sn(II) dihydride complexes required the presence of strongly Lewis acidic metal carbonyls, e.g., $\text{IPr}\cdot\text{SnH}_2\cdot\text{M}(\text{CO})_5$ ($\text{M} = \text{Cr}$ and W).^{10a,33} Overall, similar trends were found with respect to the energetics of decomposition in our $\text{NHC}\cdot\text{SnH}_2\cdot\text{BH}_3$ models (Figures S65–S69)¹⁹ as in the above-mentioned GeH_2 donor–acceptor complexes. When examining $\text{ImMe}_2\cdot\text{SnH}_2\cdot\text{BH}_3$, the biggest difference is the more facile and favorable cleavage of the Sn–B linkage in path B (90.3 kJ/mol in THF, 80.1 kJ/mol in the gas phase)¹⁹ compared to the Ge–C bond breakage in $\text{ImMe}_2\cdot\text{GeH}_2\cdot\text{BH}_3$ (122.7 kJ/mol in THF). For $\text{ImMe}_2\cdot\text{SnH}_2\cdot\text{BH}_3$, the common Sn to C_{NHC} 1,2-hydride shift in paths C and D (to give $(\text{ImMe}_2\text{H})\text{SnH}\cdot\text{BH}_3$) is substantially uphill energetically, with a free energy of activation of 192.8 kJ/mol in THF (Figure S69).¹⁹ In addition, the overall decomposition reaction associated with paths A and B, $\text{ImMe}_2\cdot$

$\text{SnH}_2\cdot\text{BH}_3 \rightarrow \text{ImMe}_2\cdot\text{BH}_3 + \text{Sn}(\text{s}) + \text{H}_2$, was estimated to have a $\Delta_{\text{decomp}}G$ value of -241.1 kJ/mol in THF (vs one of -242.9 in the absence of solvent); as for the germanium analogues, similar overall trends were found in the computed Sn(II) dihydride complexes $\text{Im}\cdot\text{SnH}_2\cdot\text{BH}_3$ and $\text{IPr}\cdot\text{SnH}_2\cdot\text{BH}_3$.¹⁹

Kinetic Analysis of the Decomposition of $\text{ImMe}_2\cdot\text{GeH}_2\cdot\text{BH}_3$ (6) and Link to Computations. Based on our computational work (*vide supra*), paths A and B are viable routes by which the elemental germanium is extruded from $\text{NHC}\cdot\text{GeH}_2\cdot\text{BH}_3$ adducts. Because we used THF as our solvent model, the decomposition of the Ge(II) hydride adduct $\text{ImMe}_2\cdot\text{GeH}_2\cdot\text{BH}_3$ (**6**) in refluxing THF-D₈ (18 h) was explored to see if the dominant product was an $\text{NHC}\cdot\text{BH}_3$ complex (arising from path A or B, Scheme 4) or a dihydroaminal [$(\text{HCNMe})_2\text{CH}_2$] (arising from path C or D, Scheme 4). After the thermolysis of **6** in THF-D₈, $\text{ImMe}_2\cdot\text{BH}_3$ was detected as a product by ¹H NMR spectroscopy (20%, determined relative to 4,4′-difluorobiphenyl as an internal standard, Figure S31);¹⁹ however, other unidentified products were also present. Interestingly, THF·BH₃ was also detected by ¹¹B NMR analysis of the end products (Figure S32),¹⁹ indicating that the coordinating solvent (THF) plays an added role in the thermal degradation of **6** by trapping some of the BH₃ that is liberated.

To recap, when $\text{ImMe}_2\cdot\text{GeH}_2\cdot\text{BH}_3$ (**6**) was heated at 100 °C in either toluene-D₈ or C₆D₆, $\text{ImMe}_2\cdot\text{BH}_3$ was found to be the only soluble decomposition product. Thus, at this point, either path A or B was likely responsible for the decomposition of **6** in weakly coordinating solvents due to the absence of the dihydroaminal degradation product [$(\text{HCNMe})_2\text{CH}_2$]. To further investigate the mechanism by which $\text{ImMe}_2\cdot\text{GeH}_2\cdot\text{BH}_3$ (**6**) decomposes, a solution of **6**³⁴ in toluene-D₈ was heated in a sealed J-Young NMR tube to 100 °C, and the progress of the decomposition was monitored *in situ* using ¹H NMR (in the presence of 4,4′-difluorobiphenyl as an internal standard). As expected for unimolecular decomposition, a linear relationship of $\ln[\mathbf{6}]$ with time was found (Figure 7), leading to a first-order rate constant (k_{H}) of $1.9(2) \times 10^{-4} \text{ s}^{-1}$. It should be stated that the observed first-order decay in **6** could fit any of the computationally investigated paths (A–D) in Scheme 4, as all

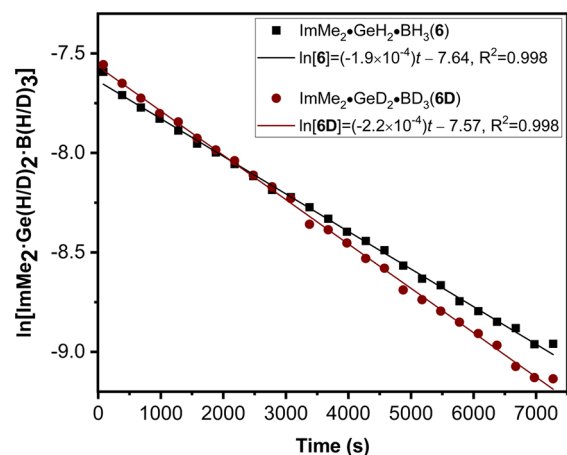


Figure 7. Decomposition rates of $\text{ImMe}_2\cdot\text{GeH}_2\cdot\text{BH}_3$ (**6**, black squares) and $\text{ImMe}_2\cdot\text{GeD}_2\cdot\text{BD}_3$ (**6D**, red circles). Each thermolysis run was conducted at 100 °C in toluene-D₈ with spectral integration relative to an internal standard of 4,4′-difluorobiphenyl. Average data points from three trials are plotted.

paths are unimolecular-based decompositions. However, one might see different kinetic isotope effects (KIEs) among the proposed decomposition pathways, as paths C and D start with a common Ge–H bond breaking event as a rate-determining step (i.e., 1,2-hydrogen shift). As a result, the deuterium isotopologue $\text{ImMe}_2\text{-GeD}_2\text{-BD}_3$ (**6D**) was prepared from $\text{ImMe}_2\text{-GeCl}_2$ and $\text{Li}[\text{BD}_4]$, and its decomposition in toluene- D_8 was examined.

The thermolysis of **6D** in toluene- D_8 (100 °C) was carried out in triplicate, leading to a rate of decomposition of $2.2(2) \times 10^{-4} \text{ s}^{-1}$ (Figure 7) and a kinetic isotope effect ($\text{KIE} = k_{\text{H}}/k_{\text{D}}$) of 0.86(11). Rate-determining hydride-transfer in path C or D would be expected to follow a normal primary KIE ($k_{\text{H}}/k_{\text{D}} \gg 1$); thus, the observed kinetic data supports that decomposition of **6** (and **6D**) via either path A or B.³⁵ Moreover, both paths A and B might yield a small inverse KIE ($k_{\text{H}}/k_{\text{D}} < 1$), as the H and D atoms are located in secondary positions in relation to the rate determining bond cleavage (C–Ge or Ge–B) involved in the decomposition.

Curious about further differentiating between paths A and B, we decided to computationally investigate the KIE associated with each path. Specifically, we aimed to determine whether an inverse KIE would be expected for these pathways due to secondary bond breakage effects. Before outlining our computational work, we would like to highlight eq 1, which links the dependence of the KIE value to changes in the kinetic energy during secondary bond breakage events³⁶

$$k_{\text{H}}/k_{\text{D}} = \exp\left\{-\frac{1}{2} \times \sum [u_{\text{H}}^{\ddagger} - u_{\text{D}}^{\ddagger} - (u_{\text{H}}^0 - u_{\text{D}}^0)]\right\} \quad (1)$$

Given that u represents the $h\nu/kT$ of the transition state (\ddagger) and the initial condition (0), and that the relationship between the vibrational frequencies of E–H and E–D bonds can be approximated as $\nu_{\text{E-D}} = \nu_{\text{E-H}}/1.35$, this expression can be simplified to eq 2, wherein the direct association of KIE to the sum of the E–H vibrational frequency changes becomes evident. When the overall change in E–H bond frequencies ($\Sigma\Delta\nu$, in cm^{-1}) becomes greater than zero ($\Sigma\Delta\nu > 0$) during complex dissociation, an inverse kinetic isotope effect can be expected (i.e., $k_{\text{H}}/k_{\text{D}} < 1$)³⁶

$$k_{\text{H}}/k_{\text{D}} = \exp\{(-0.1865/T) \times \Sigma\Delta\nu\} \quad (2)$$

Going back to the assumption that either path A or B (Ge–C or Ge–B bond cleavage, respectively) is the most likely mechanism for the decomposition of $\text{ImMe}_2\text{-GeH}_2\text{-BH}_3$ (**6**) (*vide supra*), a computational study (B3LYP/cc-pVDZ) was carried out to investigate the change in Raman frequencies of the Ge–H and B–H bonds during adduct dissociation and bond cleavage.³⁷ As the simplified expression in eq 2 relies only on the change in the vibrational frequency and already accounts for the change in mass between H and D, calculations were carried out only on the hydrogen isotopologue $\text{ImMe}_2\text{-GeH}_2\text{-BH}_3$ (**6**). Although the default temperature for the computed vibrational frequencies was 298 K¹⁹ and experimental decomposition occurred at 373 K, Raman frequencies do not shift drastically with temperature;³⁸ therefore, a comparison can be made between the computed and experimental KIE values.

For the calculations related to path A, sequential C–Ge bond extensions in 0.1 Å increments were applied starting from an optimized C–Ge bond length of 2.062 Å to a final distance of 3.062 Å (B3LYP/cc-pVDZ).¹⁹ After each bond elongation event, the new bond length was then frozen, and all other

angles and bond lengths in the molecule were optimized. Figure 8 shows the changes in the Raman resonance frequency

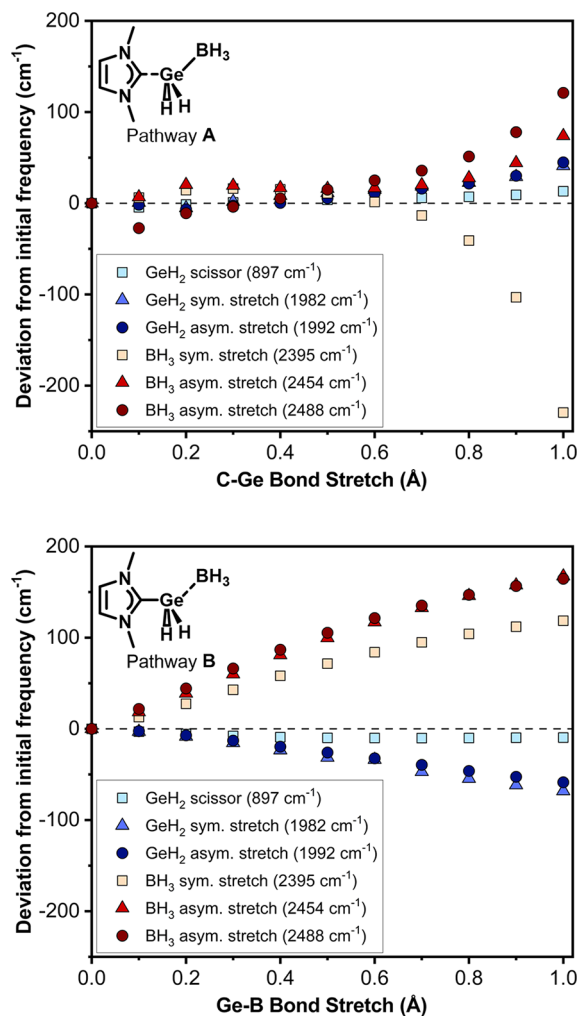


Figure 8. Deviations from the initial calculated Raman frequencies (B3-LYP/cc-pVDZ) of the BH_3 and GeH_2 resonance frequencies with increasing C–Ge (path A, starting bond length 2.010 Å) and Ge–B (path B, starting bond length 2.060 Å) bond lengths.

of the BH_3 and GeH_2 symmetric and asymmetric stretches during the ImMe_2 dissociation from $\text{ImMe}_2\text{-GeH}_2\text{-BH}_3$ (**6**). According to eq 2, the Raman frequencies should be modeled at the transition state of the bond breaking step. However, the energies associated with this dissociation confirmed the earlier assumption that the bond is broken without an energy barrier in the form of a transition state (Figure S57); therefore, the highest energy species (longest bond length) was examined for comparative purposes. The longest tested bond length had a C–Ge bond length of 3.062 Å. The sum changes in E–H frequencies at this C–Ge distance have values of -35 and $+99 \text{ cm}^{-1}$ for the B–H and Ge–H stretches, respectively. Of particular note is the strong negative contribution of the BH_3 symmetric stretching frequency, which comprises the entirety of the negative frequency contributions.³⁷ Applying eq 2 to this system ($k_{\text{H}} = 1.9 \times 10^{-4} \text{ s}^{-1}$, $\Sigma\Delta\nu = +64 \text{ cm}^{-1}$, and $T = 373 \text{ K}$), a k_{D} of $2.0 \times 10^{-4} \text{ s}^{-1}$ was expected ($\text{KIE} = 0.93$).

Path B was modeled in a similar fashion with sequential Ge–B bond extensions in 0.1 Å increments from a starting bond length of 2.010 Å to a final distance of 3.010 Å. As the BH_3

center in this model begins to rehybridize from its starting 4-coordinate sp^3 environment in **6** to an approximately planar sp^2 arrangement as the B–Ge bond lengthens, the resulting increase in s-orbital character in the B–H bonds should lead to higher B–H stretching frequencies. Accordingly, the total change in B–H stretching frequencies from the initial to final geometry was computed to be $+451\text{ cm}^{-1}$. In contrast, the overall change in Ge–H asymmetric and symmetric stretches decreased by 136 cm^{-1} ; thus, the change in the B–H stretching frequency is the dominant term (by a factor of 3). The summary large positive change in the vibrational frequencies for path B leads to an expected k_D of $2.7 \times 10^{-4}\text{ s}^{-1}$ (by eq 2, $\Sigma\Delta\nu = +314\text{ cm}^{-1}$ and $\text{KIE} = 0.82$). It should be taken into consideration that the experimental values do have an inherent error and that the rates predicted by the computational analysis fall within 3σ of the experimental values for both paths A and B. Thus, our computational analysis of the KIE is in line with the experimental data and supports the decomposition of **6** via an initial bond dissociation process, with a slight preference for path B (starting with the Ge–B bond breaking) on the basis of the computed free energies involved.

CONCLUSIONS

This work introduces new $\text{NHC}\cdot\text{GeH}_2\cdot\text{BH}_3$ donor–acceptor complexes featuring an unprecedented high Ge atom content (approaching 40 wt %). We also show that $\text{ImMe}_2\cdot\text{GeH}_2\cdot\text{BH}_3$ can deposit nanodimensional films of Ge onto silicon wafers and unusual substrates, such as glass wool, from solution via a convenient and mild ($100\text{ }^\circ\text{C}$) procedure.¹⁹ Our procedure requires only standard Schlenk techniques and glassware, and any byproducts formed during Ge film deposition can be easily removed by washing with an organic solvent. This is in contrast to pre-existing routes to Ge films that require very high temperatures or sophisticated CVD set-ups.¹³ Additionally, we examined four different decomposition pathways for various $\text{NHC}\cdot\text{EH}_2\cdot\text{BH}_3$ ($\text{E} = \text{Ge}$ and Sn) complexes, and an analysis of the computed Gibbs free energies and kinetic studies points toward the initial E–B bond cleavage as the most likely decomposition route to eventually yield $\text{NHC}\cdot\text{BH}_3$, Ge or Sn, and H_2 . Future work will involve the application of our mild Ge deposition strategy to nanochemistry (i.e., core–shell nanoparticle synthesis) and the modification of our donor–acceptor approach to enable more atom efficient element deposition cycles.

ASSOCIATED CONTENT

Supporting Information

The Supporting Information is available free of charge at <https://pubs.acs.org/doi/10.1021/acs.inorgchem.0c01492>.

Experimental details, NMR characterization, crystallographic data, characterization of the deposited Ge, computational details, and a link to output (.log) files for all computations that were conducted (PDF)

Accession Codes

CCDC 1986302–1986305 contain the supplementary crystallographic data for this paper. These data can be obtained free of charge via www.ccdc.cam.ac.uk/data_request/cif, or by emailing data_request@ccdc.cam.ac.uk, or by contacting The Cambridge Crystallographic Data Centre, 12 Union Road, Cambridge CB2 1EZ, UK; fax: + 44 1223 336033. Computa-

tional data can be downloaded free of charge from FigShare: [10.6084/m9.figshare.11962752](https://doi.org/10.6084/m9.figshare.11962752)

AUTHOR INFORMATION

Corresponding Authors

Alex Brown – Department of Chemistry, University of Alberta, Edmonton, Alberta, Canada T6G 2G2; orcid.org/0000-0002-5384-9222; Email: alex.brown@ualberta.ca

Eric Rivard – Department of Chemistry, University of Alberta, Edmonton, Alberta, Canada T6G 2G2; orcid.org/0000-0002-0360-0090; Email: erivard@ualberta.ca

Authors

Jocelyn Sinclair – Department of Chemistry, University of Alberta, Edmonton, Alberta, Canada T6G 2G2; orcid.org/0000-0001-5835-4344

Guoliang Dai – School of Chemistry, Biology and Materials Engineering, Suzhou University of Science and Technology, 2215009 Suzhou, P. R. China

Robert McDonald – Department of Chemistry, University of Alberta, Edmonton, Alberta, Canada T6G 2G2; orcid.org/0000-0002-4065-6181

Michael J. Ferguson – Department of Chemistry, University of Alberta, Edmonton, Alberta, Canada T6G 2G2; orcid.org/0000-0002-5221-4401

Complete contact information is available at: <https://pubs.acs.org/10.1021/acs.inorgchem.0c01492>

Author Contributions

The manuscript was written through contributions of all authors. J.S. contributed all experimental work, simulated Raman and kinetic studies, and contributed to the manuscript. G.D. contributed computational investigations of decomposition and rearrangement pathways. M.J.F. and R.M. provided X-ray crystallographic structure refinements. A.B. and E.R. are the principle investigators, contributing to the manuscript and the interpretation of data. All authors have given approval to the final version of the manuscript.

Funding

This work was supported by the NSERC of Canada (Discovery grants to E.R. and A.B.), NSERC CREATE funding to E.R. and J.M.S., and the National Natural Science Foundation of China (No. 21203135) for supporting G.D. J.M.S. also thanks NSERC for a CGS-M scholarship and the University of Alberta for a QE II Scholarship.

Notes

The authors declare no competing financial interest.

ACKNOWLEDGMENTS

The computational studies in this work were made possible by the Compute/Calcul Canada (www.computecanada.ca) facilities. We also thank Haoyang Yu for the SEM images, Mark Miskolzie for the high-temperature NMR data collection and discussions, Christoph Wallach and Dr. Mustafa Supur for the collection of the Raman data, Dr. Emanuel Hupf for the computational assistance with the modeling of the Raman spectra, Ian Watson for helpful suggestions, and Lorenzo Garcia for the initial work on $\text{Im}^i\text{Pr}_2\text{Me}_2\cdot\text{GeH}_2\cdot\text{BH}_3$. A.B. and G.D. thank Tyler Ries and Hanseul Kim for carrying out the exploratory computational studies on the decomposition of $\text{IPr}\cdot\text{GeH}_2\cdot\text{BH}_3$.

REFERENCES

- (1) Usually, EH_2 species are generated as mixtures with other polyhydrides. For examples, see: (a) Jasinski, J. M.; Becerra, R.; Walsh, R. Direct Kinetic Studies of Silicon Hydride Radicals in the Gas Phase. *Chem. Rev.* **1995**, *95*, 1203–1228. (b) Aldridge, S.; Downs, A. J. Hydrides of the Main-Group Metals: New Variations on an Old Theme. *Chem. Rev.* **2001**, *101*, 3305–3366. (c) Hirota, E.; Ishikawa, H. The vibrational spectrum and molecular constants of silicon dihydride SiH_2 in the ground electronic state. *J. Chem. Phys.* **1999**, *110*, 4254–4257. (d) Wang, X.; Andrews, L. Infrared Spectra of Group 14 Hydrides in Solid Hydrogen: Experimental Observation of PbH_4 , Pb_2H_2 , and Pb_2H_4 . *J. Am. Chem. Soc.* **2003**, *125*, 6581–6587. (e) Young, N. A. Main group coordination chemistry at low temperatures: A review of matrix isolated Group 12 to Group 18 complexes. *Coord. Chem. Rev.* **2013**, *257*, 956–1010.
- (2) (a) Jacobsen, H.; Ziegler, T. Transition Metal Fischer-Type Complexes. Density Functional Analysis of the Systems $(\text{CO})_5\text{CrEH}_2$ ($\text{E} = \text{C}, \text{Si}, \text{Ge}, \text{Sn}$) and $(\text{CO})_5\text{MCH}_2$ ($\text{M} = \text{Mo}, \text{W}, \text{Mn}^+$). *Inorg. Chem.* **1996**, *35*, 775–783. (b) Apeloig, Y.; Pauncz, R.; Karni, M.; West, R.; Steiner, W.; Chapman, D. Why is Methylene a Ground State Triplet while Silylene is a Ground State Singlet? *Organometallics* **2003**, *22*, 3250–3256.
- (3) (a) Jasinski, J. M.; Gates, S. M. Silicon Chemical Vapor Deposition One Step at a Time: Fundamental Studies of Silicon Hydride Chemistry. *Acc. Chem. Res.* **1991**, *24*, 9–15. (b) Grochala, W.; Edwards, P. P. Thermal Decomposition of the Non-Interstitial Hydrides for the Storage and Production of Hydrogen. *Chem. Rev.* **2004**, *104*, 1283–1316. (c) Rivard, E. Group 14 inorganic hydrocarbon analogues. *Chem. Soc. Rev.* **2016**, *45*, 989–1003.
- (4) (a) Schrock, R. R. Alkylidene Complexes of Niobium and Tantalum. *Acc. Chem. Res.* **1979**, *12*, 98–104. (b) Tebbe, F. N.; Parshall, G. W.; Ovenall, D. W. Titanium-Catalyzed Olefin Metathesis. *J. Am. Chem. Soc.* **1979**, *101*, 5074–5075. (c) Schwab, P.; France, M. B.; Ziller, J. W.; Grubbs, R. H. A Series of Well-Defined Metathesis Catalysts – Synthesis of $[\text{RuCl}_2(=\text{CHR})(\text{PR}_3)_2]$ and Its Reactions. *Angew. Chem., Int. Ed. Engl.* **1995**, *34*, 2039–2041. (d) Scott, J.; Mindiola, D. J. A tribute to Frederick Nye Tebbe. Lewis acid stabilized alkylidyne, alkylidene, and imides of 3d early transition metals. *Dalton Trans.* **2009**, 8463–8472.
- (5) (a) von Pechmann, H. Über Diazomethan. *Ber. Dtsch. Chem. Ges.* **1894**, *27*, 1888–1891. (b) Yang, H.; Martin, B.; Schenkel, B. On-Demand Generation and Consumption of Diazomethane in Multistep Continuous Flow Systems. *Org. Process Res. Dev.* **2018**, *22*, 446–456.
- (6) For the photoassisted extrusion of EH_2 units ($\text{E} = \text{Si}$ and Ge) via cyclobutane and cyclopentene analogues, see: (a) Barton, T. J.; Tillman, N. Mechanism of the Decomposition of Silacyclobutane to Silylene and Propene. *J. Am. Chem. Soc.* **1987**, *109*, 6711–6716. (b) Becerra, R.; Boganov, S. E.; Egorov, M. P.; Nefedov, O. M.; Walsh, R. Room Temperature Observation of GeH_2 and the First Time-Resolved Study of Some of Its Reactions. *Chem. Phys. Lett.* **1996**, *260*, 433–440. (c) For a computational investigation of this process, see: Su, M.-D. Excited-State Photolytic Mechanism of Cyclopentene Containing a Group 14 Element: An MP2-CAS//CASSCF Study. *J. Phys. Chem. A* **2015**, *119*, 8611–8618.
- (7) Thimer, K. C.; Al-Rafia, S. M. I.; Ferguson, M. J.; McDonald, R.; Rivard, E. Donor/acceptor stabilization of Ge(II) dihydride. *Chem. Commun.* **2009**, 7119–7121.
- (8) Rivard, E. Donor–acceptor chemistry in the main group. *Dalton Trans.* **2014**, *43*, 8577–8586.
- (9) For related studies on donor–acceptor stabilization, see: (a) Marks, T. J. Dialkylgermylene- and -stannylene-Pentacarbonylchromium Complexes. *J. Am. Chem. Soc.* **1971**, *93*, 7090–7091. (b) Schmid, G.; Welz, E. Base-Stabilized Silyleneiron Complexes. *Angew. Chem., Int. Ed. Engl.* **1977**, *16*, 785–786. (c) Petz, W. Transition-Metal Complexes with Derivatives of Divalent Silicon, Germanium, Tin, and Lead as Ligands. *Chem. Rev.* **1986**, *86*, 1019–1047. (d) Vogel, A.; Timoshkin, A. Y.; Scheer, M. Lewis Acid/Base Stabilized Phosphanylalane and -Gallane. *Angew. Chem., Int. Ed.* **2001**, *40*, 4409–4412. (e) Rugar, P. A.; Jennings, M. C.; Ragogna, P. J.; Baines, K. M. Stabilization of a Transient Diorganogermylene by an N-Heterocyclic Carbene. *Organometallics* **2007**, *26*, 4109–4111. (f) Ghadwal, R. S.; Azhakar, R.; Roesky, H. W. Dichlorosilylene: A High Temperature Transient Species to an Indispensable Building Block. *Acc. Chem. Res.* **2013**, *46*, 444–456. (g) Jana, A.; Huch, V.; Rzepa, H. S.; Scheschke, D. A Molecular Complex with a Formally Neutral Iron Germanide Motif (Fe_2Ge_2). *Organometallics* **2015**, *34*, 2130–2133. (h) Hickox, H. P.; Wang, Y.; Xie, Y.; Wei, P.; Schaefer, H. F., III; Robinson, G. H. Push–Pull Stabilization of Parent Monochlorosilylenes. *J. Am. Chem. Soc.* **2016**, *138*, 9799–9802. (i) Hegen, O.; Marquardt, C.; Timoshkin, A. Y.; Scheer, M. A Convenient Route to Mixed Pnictogenylboranes. *Angew. Chem., Int. Ed.* **2017**, *56*, 12783–12787. (j) Hegen, O.; Bräse, J.; Timoshkin, A. Y.; Scheer, M. Bidentate Phosphanyl- and Arsenylboranes. *Chem. - Eur. J.* **2019**, *25*, 485–489. (k) Tremmel, J.; Tydlitat, J.; Dostal, L.; Ruzicka, A.; Deraet, X.; Turek, J.; Jambor, R. Organogermanium(II) Hydrides as a Source of Highly Soluble LiH. *Chem. - Eur. J.* **2020**, *26*, 6070–6075.
- (10) (a) Al-Rafia, S. M. I.; Malcolm, A. C.; Liew, S. K.; Ferguson, M. J.; Rivard, E. Stabilization of the Heavy Methylene Analogues, GeH_2 and SnH_2 , within the Coordination Sphere of a Transition Metal. *J. Am. Chem. Soc.* **2011**, *133*, 777–779. (b) Al-Rafia, S. M. I.; Malcolm, A. C.; Liew, S. K.; Ferguson, M. J.; McDonald, R.; Rivard, E. Intercepting low oxidation state main group hydrides with a nucleophilic N-heterocyclic olefin. *Chem. Commun.* **2011**, *47*, 6987–6989. (c) Al-Rafia, S. M. I.; Malcolm, A. C.; McDonald, R.; Ferguson, M. J.; Rivard, E. Trapping the Parent Inorganic Ethylenes H_2SiGeH_2 and H_2SiSnH_2 in the Form of Stable Adducts at Ambient Temperature. *Angew. Chem., Int. Ed.* **2011**, *50*, 8354–8357. (d) Al-Rafia, S. M. I.; Malcolm, A. C.; McDonald, R.; Ferguson, M. J.; Rivard, E. Efficient generation of stable adducts of Si(II) dihydride using a donor–acceptor approach. *Chem. Commun.* **2012**, *48*, 1308–1310. (e) Al-Rafia, S. M. I.; Momeni, M. R.; Ferguson, M. J.; McDonald, R.; Brown, A.; Rivard, E. Stable Complexes of Parent Digermene: An Inorganic Analogue of Ethylene. *Organometallics* **2013**, *32*, 6658–6665. (f) Swarnakar, A. K.; McDonald, S. M.; Deutsch, K. C.; Choi, P.; Ferguson, M. J.; McDonald, R.; Rivard, E. Application of the Donor–Acceptor Concept to Intercept Low Oxidation State Group 14 Element Hydrides using a Wittig Reagent as a Lewis Base. *Inorg. Chem.* **2014**, *53*, 8662–8671.
- (11) Purkait, T. K.; Swarnakar, A. K.; De Los Reyes, G. B.; Hegmann, F. A.; Rivard, E.; Veinot, J. G. C. One-pot synthesis of functionalized germanium nanocrystals from a single source precursor. *Nanoscale* **2015**, *7*, 2241–2244.
- (12) Vaughn, D. D.; Schaak, R. E. Synthesis, properties and applications of colloidal germanium and germanium-based nanomaterials. *Chem. Soc. Rev.* **2013**, *42*, 2861–2879.
- (13) For related examples of Ge nanomaterial formation under harsher (thermal or reducing) conditions, see: (a) Tabatabaei, K.; Holmes, A. L.; Newton, K. A.; Muthuswamy, E.; Sfadia, R.; Carter, S. A.; Kaulzarich, S. M. Halogen-Induced Crystallinity and Size Tuning of Microwave Synthesized Germanium Nanocrystals. *Chem. Mater.* **2019**, *31*, 7510–7521. (b) Kirshenbaum, M. J.; Boebinger, M. G.; Katz, M. J.; McDowell, M. T.; Dasog, M. Solid-State Route for the Synthesis of Scalable, Luminescent Silicon and Germanium Nanocrystals. *ChemNanoMat* **2018**, *4*, 423–429. (c) Javadi, M.; Picard, D.; Sinelnikov, R.; Narreto, M. A.; Hegmann, F. A.; Veinot, J. G. C. Synthesis and Surface Functionalization of Hydride-Terminated Ge Nanocrystals Obtained from the Thermal Treatment of $\text{Ge}(\text{OH})_2$. *Langmuir* **2017**, *33*, 8757–8765. (d) Yoo, S.; Yoo, C.; Park, E.-S.; Kim, W.; Lee, Y. K.; Hwang, C. S. Chemical interactions in the atomic layer deposition of Ge–Sb–Se–Te films and their ovonic threshold switching. *J. Mater. Chem. C* **2018**, *6*, 5025–5032. (e) Nguyen, V. H.; Dobbie, A.; Myronov, M.; Norris, D. J.; Walther, T.; Leadley, D. R. Epitaxial growth of relaxed germanium layers by reduced pressure chemical vapour deposition on (110) and (111) silicon substrates. *Thin Solid Films* **2012**, *520*, 3222–3226. (f) Malaquias, J. C.; Wu, M.; Lin, J.; Robert, E. V. C.; Sniekers, J.; Binnemans, K.; Dale, P. J.; Franssaer, J. Electrodeposition of germanium-containing precursors for

Cu₂(Sn,Ge)S₃ thin film solar cells. *Electrochim. Acta* **2017**, *251*, 651–659.

(14) (a) Frey, G. D.; Masuda, J. D.; Donnadieu, B.; Bertrand, G. Activation of Si-H, B-H, and P-H Bonds at a Single Nonmetal Center. *Angew. Chem., Int. Ed.* **2010**, *49*, 9444–9447. (b) Arrowsmith, M.; Hill, M. S.; Kociok-Köhn, G.; MacDougall, D. J.; Mahon, M. F. Beryllium-Induced C-N Bond Activation and Ring Opening of an N-Heterocyclic Carbene. *Angew. Chem., Int. Ed.* **2012**, *51*, 2098–2100. (c) Schmidt, D.; Berthel, J. H. J.; Pietsch, S.; Radius, U. C-N Bond Cleavage and Ring Expansion of N-Heterocyclic carbenes using Hydrosilanes. *Angew. Chem., Int. Ed.* **2012**, *51*, 8881–8885. (d) Al-Rafia, S. M. I.; McDonald, R.; Ferguson, M. J.; Rivard, E. Preparation of Stable Low-Oxidation-State Group 14 Element Amidohydrides and Hydride-Mediated Ring-Expansion Chemistry of N-Heterocyclic Carbenes. *Chem. - Eur. J.* **2012**, *18*, 13810–13820. (e) Wang, T.; Stephan, D. W. Carbene-9-BBN Ring Expansions as a Route to Intramolecular Frustrated Lewis Pairs for CO₂ Reduction. *Chem. - Eur. J.* **2014**, *20*, 3036–3039. (f) Würtemberger-Pietsch, S.; Radius, U.; Marder, T. M. 25 years of N-heterocyclic carbenes: activation of both main-group element–element bonds and NHCs themselves. *Dalton Trans.* **2016**, *45*, 5880–5895. (g) Anker, M. D.; Colebatch, A. L.; Iversen, K. J.; Wilson, D. J. D.; Dutton, J. L.; García, L.; Hill, M. S.; Liptrot, D. J.; Mahon, M. F. Alane-Centered Ring Expansion of N-Heterocyclic Carbenes. *Organometallics* **2017**, *36*, 1173–1178. For computational studies, see: (h) Momeni, M. R.; Rivard, E.; Brown, A. Carbene-Bound Borane and Silane Adducts: A Comprehensive DFT Study on their Stability and Propensity for Hydride-Mediated Ring Expansion. *Organometallics* **2013**, *32*, 6201–6208. (i) Iversen, K. J.; Wilson, D. J. D.; Dutton, J. L. Comparison of the Mechanism of Borane, Silane, and Beryllium Hydride Ring Insertion into N-Heterocyclic Carbene C–N Bonds: A Computational Study. *Organometallics* **2013**, *32*, 6209–6217.

(15) (a) Becerra, R.; Boganov, S. E.; Egorov, M. P.; Faustov, V. I.; Nefedov, O. M.; Walsh, R. The Prototype Ge-H Insertion Reaction of Germylene with Germane. Absolute Rate Constants, Temperature Dependence, RRKM Modeling and the Potential Energy Surface. *J. Am. Chem. Soc.* **1998**, *120*, 12657–12665. (b) Billone, P. S.; Beleznyay, K.; Harrington, C. R.; Huck, L. A.; Leigh, W. J. A Glimpse at the Chemistry of GeH₂ in Solution. Direct Detection of an Intramolecular Germylene–Alkene π -Complex. *J. Am. Chem. Soc.* **2011**, *133*, 10523–10534.

(16) Kuhn, N.; Kratz, T. Synthesis of Imidazol-2-ylidenes by Reduction of Imidazole-2(3H)-thiones. *Synthesis* **1993**, 561–562.

(17) (a) Prabusankar, G.; Sathyanarayana, A.; Suresh, P.; Naga Babu, C.; Srinivas, K.; Metla, B. P. R. N-heterocyclic carbene supported heavier group 14 elements: Recent progress and challenges. *Coord. Chem. Rev.* **2014**, *269*, 96–133. (b) Nesterov, V.; Reiter, D.; Bag, P.; Frisch, P.; Holzner, R.; Porzelt, A.; Inoue, S. NHCs in Main Group Chemistry. *Chem. Rev.* **2018**, *118*, 9678–9842.

(18) Coyle, J. P.; Sirianni, E. R.; Korobkov, I.; Yap, G. P. A.; Dey, G.; Barry, S. T. Study of Monomeric Copper Complexes Supported by N-Heterocyclic and Acyclic Diamino Carbenes. *Organometallics* **2017**, *36*, 2800–2810.

(19) For full computational, experimental, and crystallographic details, see the [Supporting Information](#). CCDC entries 1986302–1986305 contain the supplementary crystallographic data for this paper. These data are provided free of charge from The Cambridge Crystallographic Data Centre.

(20) Al-Rafia, S. M. I.; Lummis, P. A.; Swarnakar, A. K.; Deutsch, K. C.; Ferguson, M. J.; McDonald, R.; Rivard, E. Preparation and Structures of Group 12 and 14 Element Halide-Carbene Complexes. *Aust. J. Chem.* **2013**, *66*, 1235–1245.

(21) Rugar, P. A.; Staroverov, V. N.; Ragogna, P. J.; Baines, K. M. A Germanium(II)-Centered Dication. *J. Am. Chem. Soc.* **2007**, *129*, 15138–15139.

(22) Böttcher, T.; Bassil, B. S.; Röschenhaler, G.-V. Complexes of Ge(IV)- and Sn(IV)-Fluorides with Cyclic and Acyclic Carbenes: Bis(dialkylamino)-difluoromethylenes as Carbene Sources. *Inorg. Chem.* **2012**, *51*, 763–765.

(23) Güizado-Rodríguez, M.; Ariza-Castolo, A.; Merino, G.; Vela, A.; Noth, H.; Bakmutov, V. I.; Contreras, R. Weak Intramolecular Proton-Hydride and Proton-Fluoride Interactions: Experimental (NMR, X-ray) and DFT Studies of the Bis(NBH₃) and Bis(NBF₃) Adducts of 1,3-Dimethyl-1,3-diazolidine. *J. Am. Chem. Soc.* **2001**, *123*, 9144–9152.

(24) (a) van der Eide, E. F.; Liu, T.; Camaioni, D. M.; Walter, E. D.; Bullock, R. M. Facile Thermal W–W Bond Homolysis in the N-Heterocyclic Carbene Containing Tungsten Dimer [CpW(CO)₂(IME)]₂. *Organometallics* **2012**, *31*, 1775–1789. (b) Doddi, A.; Peters, M.; Tamm, M. *Chem. Rev.* **2019**, *119*, 6994–7112.

(25) Ruddy, A. J.; Rugar, P. A.; Bladec, K. J.; Allan, C. J.; Avery, J. C.; Baines, K. M. On the Bonding in N-Heterocyclic Carbene Complexes of Germanium(II). *Organometallics* **2010**, *29*, 1362–1367.

(26) Bentlohner, M. M.; Waibel, M.; Zeller, P.; Sarkar, K.; Müller-Buschbaum, P.; Fattakhova-Rohlfing, D.; Fässler, T. F. Zintl Clusters as Wet-Chemical Precursors for Germanium Nanomorphologies with Tunable Composition. *Angew. Chem., Int. Ed.* **2016**, *55*, 2441–2445.

(27) Walton, J. C.; Brahmi, M. M.; Fensterbank, L.; Lacôte, E.; Malacria, M.; Chu, Q.; Ueng, S.-H.; Solov'yev, A.; Curran, D. P. EPR studies of the Generation, Structure, and Reactivity of N-Heterocyclic Carbene Borane Radicals. *J. Am. Chem. Soc.* **2010**, *132*, 2350–2358.

(28) (a) Whiteside, P. J. D.; Chinini, J. A.; Hunt, H. K. Techniques and Challenges for Characterizing Metal Thin Films with Applications in Photonics. *Coatings* **2016**, *6*, 35–61. (b) Shi, Q.; Roux, R.; Latourte, F.; Hild, F.; Loissard, D.; Brynaert, N. Measuring topographies from conventional SEM acquisitions. *Ultramicroscopy* **2018**, *191*, 18–33.

(29) Ratsch, C.; Venables, J. A. Nucleation theory and the early stages of thin film growth. *J. Vac. Sci. Technol., A* **2003**, *21*, S96–S109.

(30) Zhao, Y.; Truhlar, D. The M06 suite of density functionals for main group thermochemistry, thermochemical kinetics, noncovalent interactions, excited states, and transition elements: two new functionals and systematic testing of four M06-class functionals and 12 other functionals. *Theor. Chem. Acc.* **2008**, *120*, 215–241.

(31) (a) Dunning, T. H., Jr. Gaussian basis sets for use in correlated molecular calculations. I. The atoms boron through neon and hydrogen. *J. Chem. Phys.* **1989**, *90*, 1007–1023. (b) Wilson, A. K.; Woon, D. E.; Peterson, K. A.; Dunning, T. H., Jr. Gaussian basis sets for use in correlated molecular calculations. IX. The atoms gallium through krypton. *J. Chem. Phys.* **1999**, *110*, 7667–7676.

(32) (a) Wagman, D. D., Evans, W. H., Parke, V. B., Schumm, R. H., Halow, I., Bailey, S. M., Churney, K. L., Nuttall, R. L. *J. Phys. Chem. Ref. Data*, Vol. 11, Suppl. No. 2. American Chemical Society and American Institute of Physics, Washington, D. C. 1982 (b) <https://srdata.nist.gov/JPCRD/jpcrdS2Vol11.pdf> (accessed July 13, 2020).

(33) Al-Rafia, S. M. I.; Shynkaruk, O.; McDonald, S. M.; Liew, S. K.; Ferguson, M. J.; McDonald, R.; Herber, R. H.; Rivard, E. Synthesis and Mössbauer Spectroscopy of Formal Tin(II) Dichloride and Dihydride Species Supported by Lewis Acids and Bases. *Inorg. Chem.* **2013**, *52*, 5581–5589.

(34) The concentration of **6** was determined by integration of the initial ¹H NMR resonances related to 4,4-difluorobiphenyl as an internal standard.

(35) Shen, G.-B.; Xia, K.; Li, X.-T.; Li, J.-L.; Fu, Y.-H.; Yuan, L.; Zhu, X.-Q. Prediction of Kinetic Isotope Effects for Various Hydride Transfer Reactions using a New Kinetic Model. *J. Phys. Chem. A* **2016**, *120*, 1779–1799.

(36) (a) Lee, I. Secondary kinetic isotope effects involving deuterated nucleophiles. *Chem. Soc. Rev.* **1995**, *24*, 223–229. (b) Streitwieser, A.; Jagow, R. H.; Fahey, R. C.; Suzuki, S. Kinetic Isotope Effects in the Acetolyses of Deuterated Cyclopentyl Tosylates. *J. Am. Chem. Soc.* **1958**, *80*, 2326–2332.

(37) In this analysis and discussion of the change in Ge–H and B–H stretching frequencies, we focused on the isolated Ge–H and B–H stretches (three for each bond type) and did not include the impact of coupled Ge–H and B–H modes. When one does consider the impact of such coupled stretches, only modest overall changes in frequency (from 5 to 520 cm⁻¹) were seen at the various bond elongations

investigated; thus, contributions from the coupled modes were ignored.

(38) (a) Fujioka, Y. Influence of temperature on Raman lines. *Nature* **1929**, *124*, 11. (b) Venkateswarlu, K. Temperature Dependence of the Intensities of Raman Lines. *Nature* **1947**, *159*, 96–97. (c) Jehlička, J.; Edwards, H. G. M.; Culka, A. Using portable Raman spectrometers for the identification of organic compounds at low temperatures and high altitudes: exobiological applications. *Philos. Trans. R. Soc., A* **2010**, *368*, 3109–3125.